

Interband and intraband (Drude) contributions to femtosecond laser absorption in aluminum

D. Fisher,* M. Fraenkel, Z. Henis, E. Moshe, and S. Eliezer

Department of Plasma Physics, Soreq NRC, Yavne 81800, Israel

(Received 28 February 2001; revised manuscript received 23 August 2001; published 17 December 2001)

Theoretical and experimental investigations of the absorption in metallic aluminum of femtosecond-laser radiation pulses with peak intensity $I_0 \leq 10^{15}$ W/cm² are reported. Energy balance equations are solved for electron and phonon subsystems, together with Helmholtz equation for the laser radiation. Expressions for the relaxation times as functions of electron and phonon temperatures are obtained, with no free parameters. Contrary to the assumption made in published studies, we find that the interband rather than the intraband (Drude) absorption plays the dominant role in the near infrared and throughout the visible region at low and moderate intensities. For 50 fs, 800 nm laser pulses the absorption in interband transitions dominates for intensities up to few times 10^{13} W/cm². For such pulses, broadening of the parallel-band interband absorption line with the increase in electron and phonon temperatures results, for $I_0 \leq 5 \times 10^{13}$ W/cm², in the decrease of the absorption coefficient compared to the room-temperature value. In this paper, we present both the first theoretical prediction and the first experimental observation of this phenomenon. Dielectric permittivity gradients within the skin layer also contribute to the decrease in absorption. The mechanisms of the lattice disordering are considered quantitatively, and it is shown that for $I_0 < 10^{14}$ W/cm² melting does not occur in the laser-pulse duration. Experimental results are presented for 800 and 400 nm wavelengths. The agreement between the theory and the experiment is very good.

DOI: 10.1103/PhysRevE.65.016409

PACS number(s): 52.50.Jm, 78.20.-e

I. INTRODUCTION

The development of ultrashort high-power lasers has opened possibilities for a fundamental investigation of the electronic properties of solids. Several studies have shown that measurements of the optical constants (reflectivity, transmissivity) of metals shed light on nonequilibrium phenomena in condensed matter. It was pointed out by Anisimov *et al.* [1,2] that absorption of subpicosecond laser light in metals might lead to a transiently higher electron temperature compared to the lattice temperature. During the laser pulse, the radiation energy is deposited into the free-electron subsystem. In a subpicosecond laser pulse, it is possible to heat the electron gas to a temperature of several eV for a few ps while the lattice temperature remains relatively low. Indeed, the electrons cooling by energy transfer to the lattice occurs on a longer (picosecond) time scale. The lattice heating occurs on a time scale longer yet (~ 10 ps), owing to the lattice heat capacity being 1–2 orders of magnitude larger than the free-electron heat capacity as long as the free electrons are degenerate. The equilibration of the electronic system with the lattice is determined by electron-phonon (e-ph) relaxation mechanism. A detailed understanding of e-ph and electron-electron (e-e) scattering is crucial and has been the subject of many studies, since these processes determine various fundamental and technological properties of solids, material properties, such as electron and thermal transport, equation of state, and phase transitions. A transient nonequilibrium temperature difference between electrons and lattice in metals irradiated by 75 fs optical pulses was determined with pump-probe measurements [3]. The resistivity of alumi-

num in the temperature range 1–100 eV was determined from the reflectivity of a subpicosecond ultraviolet laser [4,5]. The thermal response and the optical damage of metals irradiated by ultrashort laser pulses were considered both theoretically and experimentally [6–8].

Measurements of the absorption of 120 fs, 400 nm laser pulses in a variety of solid targets, irradiated over an intensity range of 10^{13} – 10^{18} W/cm², were reported by Price *et al.* [9]. The results of these measurements at low and moderate intensities were modeled by intraband (Drude) absorption for simple metals, such as aluminum. For these metals, the absorption increases monotonically with the laser intensity I_0 up to several times 10^{14} W/cm² and then decreases, indicating the transition from solid to plasma. Other target materials, such as Cu, Au, and Ta, show additional absorption beyond Drude absorption. At high intensities ($I_0 > 10^{15}$ W/cm²), all target materials were found to reach [9] a “universal plasma mirror” state [10] and reflected about 90 % of the incident light. Non-Drude dielectric constants were also reported to explain time-resolved reflectivity measurements of tungsten targets, irradiated by 90 fs, 620 nm pulses [11].

In this paper, we present the first theoretical prediction and the first experimental observation of the effects of the interband absorption in addition to Drude absorption in aluminum irradiated by 800 and 400 nm, 50 fs laser pulses at normal incidence over an intensity range of 10^{11} to 10^{15} W/cm². Moreover, the interband absorption is dominant at low and moderate laser intensities throughout the visible and the near-infrared part of the spectrum. As it will be shown below, in the vicinity of a 800 nm wavelength, the interband absorption decreases with increasing temperature. This leads to a *decrease* in the absorption coefficient A below its room-temperature values, at a laser intensity up to 5×10^{13} W/cm². For higher intensities, up to I_0

*Also at Weizmann Institute of Science, Rehovot 76100, Israel.
Email address: fndima@plasma-gate.weizmann.ac.il

$\sim 10^{15}$ W/cm², the absorption is dominated by inverse bremsstrahlung (Drude), and A increases rapidly. The minimum of $A(I_0)$ is found near $I_0 \approx (1-2) \times 10^{13}$ W/cm². At $I_0 > 10^{15}$ W/cm², as predicted by the conventional theories, A starts to decrease again. Our theoretical analysis suggests that in aluminum the described phenomenon of the decrease in A with I_0 for $I_0 \leq 10^{13}$ W/cm² must be pronounced, for similar laser pulse duration, in the wavelength range of 750–870 nm and is strongest near 800 nm.

II. THEORY

In a metal irradiated by a fs laser pulse, the temperature T_e of the electrons in the conduction band and the temperature T_i of the ion lattice (i.e., of the phonons) can differ by orders of magnitude. This is due to a relatively low rate of energy exchange between the electrons (which absorb the laser radiation) and the lattice. The rate of energy exchange within the electron subsystem, on the other hand, is of the order of 10^{14} s⁻¹ or higher for $T_e \geq 1$ eV. Thus, the electrons may be considered to be in a local thermodynamic equilibrium and therefore may be characterized by a certain temperature. (Indeed, for fs-laser intensities so low that T_e stays significantly below 1 eV, the absorption coefficient remains essentially unchanged. The effects of the delayed thermalization of conductivity electrons may be detected by transmission spectroscopy near the absorption edge [12], but in absolute terms, the effect on A of the electron distribution deviation from equilibrium is quite small). At the temperatures considered, both the equilibrium phonon distribution and the distribution of phonons emitted by electrons is approximately uniform over all modes (except the modes with the smallest wave numbers which, under present conditions, play no role), so the phonons may be characterized by a temperature T_i . Thus, in order to model the dependence of the absorption coefficient on the laser intensity, the following set of equations [2] may be used:

$$C_e(T_e) \frac{\partial T_e}{\partial t} = \frac{\partial}{\partial x} \left(\kappa(T_e) \frac{\partial T_e}{\partial x} \right) - U(T_e, T_i) + Q(x, t), \quad (1)$$

$$C_i(T_i) \frac{\partial T_i}{\partial t} = U(T_e, T_i). \quad (2)$$

Here, C_e and C_i are the electron and the ion (i.e., phonon) heat capacities, κ is the electron heat conductivity, U is the heat transfer rate from electrons to ions (phonons), and Q is the heat deposition rate due to the laser radiation absorption. The properties of the irradiated metal change significantly on scale of 10 nm, i.e., on the skin depth scale. Thus, the heat deposition profile must be determined rigorously from

$$Q(x) = \frac{1}{2} F_z^2(x) \text{Re}\{\sigma(\omega; x)\}. \quad (3)$$

Here, $F_z(x)$ is the radiation field amplitude at the depth x inside the target, y and z are the coordinate axes parallel to the target surface, and $\sigma(x; \omega)$ is the conductivity of the

target at the incident radiation frequency ω , at the depth x . For a monochromatic wave, in order to find $F_z(x)$, the Helmholtz equation

$$\frac{\partial^2}{\partial x^2} F_z(x) + \varepsilon(\omega; x) \frac{\omega^2}{c^2} F_z(x) = 0 \quad (4)$$

must be solved [5,13] simultaneously with Eqs. (1) and (2). Here, $\varepsilon(\omega; x)$ is the dielectric permittivity of the target,

$$\varepsilon(\omega; x) = 1 + i \frac{4\pi}{\omega} \sigma(\omega; x). \quad (5)$$

Note that $\sigma(\omega; x)$ and $F_z(x)$ vary with time t on the time scale much longer than $2\pi/\omega$. Both σ and ε depend on x and t through $T_e(x, t)$ and $T_i(x, t)$, while Q and F_z^2 depend on t also via the laser-pulse temporal intensity profile

$$I(t) \approx I_0 \sin^2(\pi t/2\tau), \quad 0 \leq t \leq 2\tau, \quad (6)$$

where τ is the FWHM pulse duration. The absorption coefficient A , measured at a given location (y, z) on the target surface, is averaged over the temporal pulse profile. It is evaluated as

$$A = \frac{\int_0^{2\tau} dt \int_0^\infty Q(x, t) dx}{\int_0^{2\tau} I(t) dt}. \quad (7)$$

The absorption coefficient is related to reflectivity by $A = 1 - R$.

We consider three distinct processes contributing to the laser light absorption in metal: intraband absorption due to e-ph collisions, intraband absorption due to e-e collisions, and interband absorption [normal or parallel band (PB)]. All these mechanisms contribute to σ , and thus, also to the dielectric permittivity (5) of the metal. It will be shown below that for near-infrared and visible radiation absorption in aluminum at near-room temperature, the effect of interband absorption is dominant, while for surface electron temperature of 2–3 eV and higher (which corresponds, for a 50 fs pulse, to $I_0 > 10^{13}$ W/cm²) the “conventional” intraband absorption dominates. The interplay between the inter- and intraband absorption mechanisms leads, in aluminum, to a unique effect of absorption coefficient reduction pronounced in the fs-laser intensities range of 10^{10} – 5×10^{13} W/cm². In the present paper, we report both an experimental observation and a theoretical description of this effect.

In order to find the absorption coefficient value (7), we solve numerically the set of Eqs. (1)–(5). Towards that end, the functional dependence of C_e , C_i , κ , U , σ on the temperatures $T_e(x, t)$ and $T_i(x, t)$ must be determined first. In the present paper, we are focusing on the effect of the laser pulses of a duration less than 100 fs. For such a short pulse, the ionic structure of the target remains unchanged, unless the electron-impact ionization occurs at a rate sufficient to increase perceptibly the average ionization degree of the lat-

tice ions. In metallic Al, the average ionization degree of the lattice ions is $Z=3$, see Refs. [14–16]. The ionization threshold for the fourth electron is about 120 eV [17]. Using the electron-impact ionization cross section, as given by a fitting formula in Ref. [18], we find the average lifetime of an ion Al^{3+} with respect to electron-impact ionization to be longer than 1 ps for $T_e=20$ eV, about 200 fs for $T_e=30$ eV, and about 30 fs for $T_e=50$ eV. Thus, for $T_e < 30$ eV, we can ignore the electron-impact ionization. The thermal expansion of the outer (irradiated) target layer, for $T_e < 30$ eV, occurs on the time scale longer than the pulse duration τ . Indeed, the thickness of the layer strongly heated by radiation is of the order of 10 nm (skin depth); the shift of the outermost layer of ions with time t is approximately given by $v_s t \approx t \sqrt{\gamma Z K_B T_e / M_i}$, where v_s is the velocity of the free surface, M_i is the ion mass, $\gamma \approx 5/3$ is the adiabatic constant, and K_B is the Boltzmann constant. Even for maximal electron temperature considered, $T_e=30$ eV, we find that during the peak of the laser pulse, $t=50$ fs, the outer layer of ions shifts by ~ 1 nm. Since there are tens of atomic layers per one skin depth, the distance between the layers changes only by a fraction of angstrom. The lattice constant of Al is approximately four angstrom, therefore, during the laser pulse it is possible to neglect the effect of the lattice expansion on the phononic spectrum, band structure, and e-ph coupling. Of course, the change in the phonon mode populations due to the lattice heating must be accounted for.

We note that even in the cases when the free-electron-impact ionization and the outer-target layer expansion do not affect the target skin layer lattice structure, the lattice structure may still be destroyed by the ultrafast melting (see, for example, Ref. [11]). At the end of this section we show that this effect, too, is unimportant for 50 fs laser pulses at peak intensities up to 10^{14} W/cm².

The electron heat capacity C_e for $K_B T_e \ll E_F$ (degenerate electron gas in aluminum) is given by $C_{e \text{ low } T}(T_e) \approx 1.3 \times 10^3 T_e$ in units of erg/cm³ K [14]. For $K_B T_e > E_F$, C_e is given by $C_{e \text{ high } T}(T_e) \rightarrow 1.5 K_B n_e$ (nondegenerate free-electron gas). Here, $E_F \approx 11.7$ eV is the Fermi energy. In the intermediate region, $K_B T_e \sim E_F$, we use the interpolation formula

$$C_e(T_e) = \frac{C_{e \text{ high } T} C_{e \text{ low } T}}{\sqrt{C_{e \text{ high } T}^2 + C_{e \text{ low } T}^2}}, \quad (8)$$

which reproduces quite well the true behavior of the heat capacity of the free-electron gas in the intermediate region. The ion heat conductivity was inferred directly from the phonon spectrum, and it turns out to be quite close to the Dulong-Petit limit $C_i = 3 K_B n_i$ for $T_i \geq 300$ K. In our calculations the fitting formula $C_i(T_i) = 3 K_B n_i (1 - 4.4 \times 10^3 T_i^{-2})$ was used. Here, n_i and n_e are the number densities of ions and conductivity electrons, respectively, related by $n_e = Z n_i$.

To find κ , U , and σ as functions of T_e and T_i , we first note that the e-ph scattering in metals occurs primarily in the events of a single longitudinal phonon absorption or emis-

sion by an electron [19,20]. The exact spectrum $\omega_{ph}(q)$ of longitudinal phonons [21] may be approximated by

$$\begin{aligned} \omega_{ph} &= q s & \text{for } q \leq q_b, \\ \omega_{ph} &= q_b s & \text{for } q \geq q_b, \end{aligned} \quad (9)$$

where $s \approx 6.4 \times 10^5$ cm/s is the longitudinal sound velocity and q is the phonon wave vector. The value of q_b is determined here by fitting the electron momentum relaxation rate to the dc conductivity data, as explained below. The e-ph interaction matrix element squared is approximated by

$$\begin{aligned} |M_{\mathbf{k} \rightarrow \mathbf{k}', \pm \mathbf{q}}|^2 &= \frac{\hbar \Xi^2}{2 \rho V s} q \delta_{\mathbf{k}' - \mathbf{k}, \mp \mathbf{q}} & \text{for } q \leq q_b, \\ |M_{\mathbf{k} \rightarrow \mathbf{k}', \pm \mathbf{q}}|^2 &= \frac{\hbar \Xi^2}{2 \rho V s} q_b \delta_{\mathbf{k}' - \mathbf{k}, \mp \mathbf{q}} & \text{for } q \geq q_b, \end{aligned} \quad (10)$$

see Ref. [20], where Ξ is the deformation potential constant, ρ and V are the sample density and volume, and $\hbar \mathbf{q}$ is the quasimomentum of the phonon absorbed or emitted as the electron wave vector has changed from \mathbf{k} to \mathbf{k}' . The plus sign in $M_{\mathbf{k} \rightarrow \mathbf{k}', \pm \mathbf{q}}$ subscript stands for emission, minus sign - for absorption. The transition probability is given by

$$\begin{aligned} W_{\mathbf{k} \rightarrow \mathbf{k}', \pm \mathbf{q}} &= \frac{2 \pi}{\hbar} |M_{\mathbf{k} \rightarrow \mathbf{k}', \pm \mathbf{q}}|^2 \left(N_{\mathbf{q}} + \frac{1}{2} \pm \frac{1}{2} \right) \\ &\times \delta[E_{\mathbf{k}} - E_{\mathbf{k}'} \mp \hbar \omega_{ph}(q)]. \end{aligned} \quad (11)$$

We emphasize that \mathbf{q} may lie outside the first Brillouin zone (Umklapp process), but q_b is always inside the first Brillouin zone. In fact, the scattering in Al at room temperature and above is dominated by Umklapp, since the characteristic momentum transfer in a single collision is then $q \approx k_F$, and the Fermi surface of Al lies entirely outside the first Brillouin zone. Here, $E_{\mathbf{k}}$ is the energy of an electron with wave-vector \mathbf{k} , and $N_{\mathbf{q}}$ is the population of the longitudinal phonon mode \mathbf{q} . The wave-vector \mathbf{q} corresponds to the reduced wave-vector $\mathbf{q}_{red} = \mathbf{q} - \mathbf{K}$ in the first Brillouin zone; \mathbf{K} here is the corresponding vector of the reciprocal lattice. $N_{\mathbf{q}} = 1/(\exp\{\beta_i \hbar \omega_{ph}(q_{red})\} - 1)$, where $\beta_i = (K_B T_i)^{-1}$.

In aluminum, the density of electron states below $k = k_F$ is quite similar to that of the free electrons, therefore, the Fermi energy $E_F \approx \hbar^2 k_F^2 / 2 m_e$ where m_e is the mass of a free electron. However, the density of states in the vicinity of the Fermi surface, $k \approx k_F$, is somewhat different from that for free electrons [22]. Consequently, for $|E_{\mathbf{k}} - E_F| \ll E_F$ the electron energy $E_{\mathbf{k}} \approx E_F + \hbar^2 k_F (k - k_F) / m_{opt}$, and the Fermi velocity $v_F = (dE_{\mathbf{k}} / dk) / \hbar \approx \hbar k_F / m_{opt}$, where m_{opt} is slightly larger than m_e . The same effective mass m_{opt} enters also the expressions for U and σ . Values of m_{opt} ranging from 1.15–1.67 m_e are found in literature [15], as well as $m_{opt} = m_e$ approximation. We use $m_{opt} = 1.20 m_e$, which agrees well with the measured room-temperature reflectivity of our samples.

The rate of e-ph energy exchange was evaluated by the method described in Ref. [19], using the phonon dispersion relation (9) and the matrix element (10). We have found

$$U = \frac{2\hbar s \Xi^2 m_{opt}^2}{(2\pi\hbar)^3 \rho} \left\{ (\beta_e \hbar s)^{-5} \int_0^{\beta_e \hbar q_b s} \frac{x^4 dx}{e^x - 1} - (\beta_i \hbar s)^{-5} \int_0^{\beta_i \hbar q_b s} \frac{x^4 dx}{e^x - 1} + \frac{q_b^3}{2} [(2k_F)^2 - q_b^2] \times \left(\frac{1}{\exp\{\beta_e \hbar q_b s\} - 1} - \frac{1}{\exp\{\beta_i \hbar q_b s\} - 1} \right) \right\}. \quad (12)$$

The terms proportional to $(2k_F)^2$ are dominant at room temperature and above. U is often represented as $U = (T_e - T_i)g$, where g is a smooth function of T_e and T_i , nonzero at $T_e = T_i \neq 0$. For $T_i \geq 300$ K the expression (12) yields $g = (3.7-3.9) \times 10^{18}$ erg/(cm³ s K) nearly constant in both T_e and T_i . This value of g is in excellent agreement with that given in [11], and is by a factor of 1.5–3 larger than the empirical values used in Ref. [13].

The electron heat conductivity is given by

$$\kappa(T_e, T_i) = \frac{C_e \bar{v}^2}{3\nu}, \quad (13)$$

where \bar{v}^2 is the characteristic value of the electron velocity square, given approximately by $\bar{v}^2 \approx v_F^2 + 3K_B T_e/m_e$. The total momentum relaxation rate for electrons is given by

$$\nu = \nu_{e,ph}(T_e, T_i) + \nu_{e,e}(T_e), \quad (14)$$

where $\nu_{e,ph}$ and $\nu_{e,e}$ are the electron momentum relaxation rates due to e-ph and e-e collisions, respectively. $\nu_{e,ph}$ is given [20] by

$$\nu_{e,ph} = \sum_{\mathbf{k}'} \frac{(\mathbf{k} - \mathbf{k}') \cdot \mathbf{k}}{k^2} W_{\mathbf{k} \rightarrow \mathbf{k}', \pm \mathbf{q}} \frac{1 - f_T(\mathbf{k}')}{1 - f_T(\mathbf{k})}, \quad (15)$$

where $+\mathbf{q}$ and $-\mathbf{q}$ cases correspond to $k' \leq k$ and $k' \geq k$, respectively, and $f_T(\mathbf{k}) = 1/(\exp\{\beta_e[E_{\mathbf{k}} - \mu(T_e)]\} + 1)$, where $\mu(T_e)$ is the free-electron chemical potential and $\beta_e = (K_B T_e)^{-1}$. The detailed calculations yield, for $K_B T_e \ll E_F$ and $k \approx k_F$,

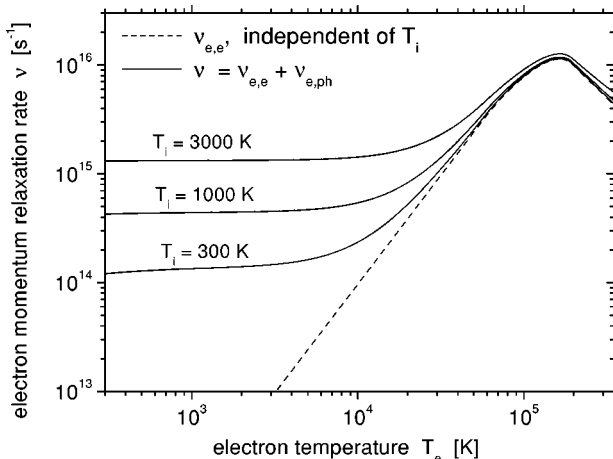


FIG. 1. Dependence of ν on T_e and T_i .

$$\nu_{e,ph} = \frac{\Xi^2}{8\pi E_F k_F \rho s} \frac{m_{opt}}{m_e} \times \left\{ \int_0^{q_b} \frac{\exp\{\beta_i \hbar q s\} + \exp\{\beta_e \hbar q s\}}{(\exp\{\beta_i \hbar q s\} - 1)(\exp\{\beta_e \hbar q s\} + 1)} q^4 dq + \eta \int_0^{q_b} \frac{\exp\{\beta_i \hbar q s\} - \exp\{\beta_e \hbar q s\}}{(\exp\{\beta_i \hbar q s\} - 1)(\exp\{\beta_e \hbar q s\} + 1)} q^3 dq + \frac{\exp\{\beta_i \hbar q_b s\} + \exp\{\beta_e \hbar q_b s\}}{(\exp\{\beta_i \hbar q_b s\} - 1)(\exp\{\beta_e \hbar q_b s\} + 1)} q_b + \frac{(2k_F)^4 - q_b^4}{4} - \eta \times \frac{\exp\{\beta_i \hbar q_b s\} - \exp\{\beta_e \hbar q_b s\}}{(\exp\{\beta_i \hbar q_b s\} - 1)(\exp\{\beta_e \hbar q_b s\} + 1)} q_b^2 (2k_F)^2 \right\}, \quad (16)$$

where $\eta = 2m_{opt}s/\hbar \ll q_b < k_F$. The first two terms are dominant at low temperatures ($\beta_e \hbar q_b s \gg 1$ and $\beta_i \hbar q_b s \gg 1$); at room temperature and above, only the last two terms are important. At higher T_e and T_i , one finds the usual dependence $\nu_{e,ph} \sim T_i$, independent of T_e [6]. For $K_B T_e \gtrsim E_F$ the above expression is no longer accurate, but in that domain, $\nu_{e,ph}$ is significantly smaller than the momentum relaxation rate in e-e collisions,

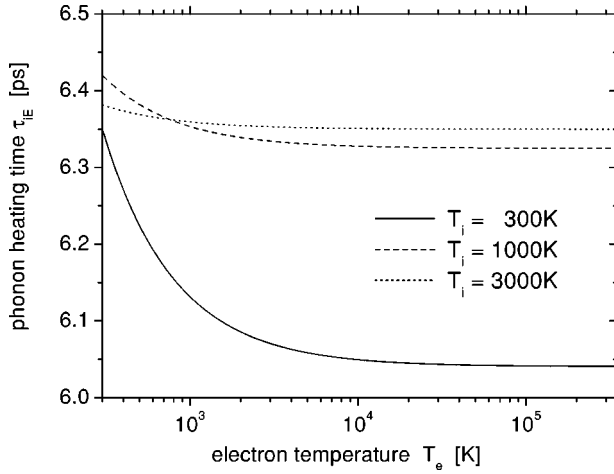
$$\nu_{e,e} \approx \frac{E_F}{\hbar} \left(\frac{K_B T_e}{E_F} \right)^2 \quad \text{for } K_B T_e \lesssim E_F, \quad (17)$$

see, e.g., Ref. [23]. At even higher temperatures, $\nu_{e,e}$ behaves according to the plasma law,

$$\nu_{e,e} \approx \frac{E_F}{\hbar} \left(\frac{K_B T_e}{E_F} \right)^{-3/2}, \quad (18)$$

where we have used the continuity of $\nu_{e,e}$ and ignored the factor logarithmic in T_e in the last expression [6]. In reality, not only $\nu_{e,e}$ but also $d\nu_{e,e}/dT_e$ must be continuous in the vicinity of $K_B T_e = E_F$, thus, we have used a third-order polynomial to smoothly interpolate $\nu_{e,e}(T_e)$ between $K_B T_e$ values of 5 and 17 eV.

Using expression (14) for ν , the exact values of Ξ^2 and q_b were determined by fitting the tabulated data [16] on dc resistivity $\sigma_{DC} = n_e e^2 / m_{opt} \nu$, at $T_e = T_i$. We have found, for $m_{opt} = 1.20m_e$, the values $\Xi = 5.162$ eV and $q_b = 4.769 \times 10^7$ cm⁻¹. Figure 1 shows ν given by Eq. (14) as the function of T_e for several values of T_i . The characteristic time scale for electron momentum relaxation is given by ν^{-1} , and varies from ~ 8 fs at room temperature (dominated by e-ph collisions) to ~ 0.1 fs at $K_B T_e \sim E_F$ (dominated by e-e collisions). The characteristic time of free electrons cooling is given by $\tau_{eE} = C_e/g \equiv C_e(T_e - T_i)/U$, and grows from ~ 100 fs at room temperature to ~ 10 ps at $K_B T_e \sim E_F$ primarily due to an increase in $C_e(T_e)$. The characteristic time of lattice heating $\tau_{iE} = C_i/g$ equals 6–6.5 ps regardless of T_e and T_i values, as both C_i and g are nearly

FIG. 2. Dependence of τ_{iE} on T_e and T_i .

constant in T_e and T_i at room temperature and above. Figure 2 shows τ_{iE} as a function of T_e and T_i . We note that, owing to τ_{iE} being nearly constant, for moderate intensities (when $K_B T_e \sim E_F$ and $C_e \approx C_i$ at the pulse peak and later) the solution of Eq. (2) for $t \sim \tau \ll \tau_{iE}$ may be approximated analytically by $T_i(t) \approx T_i(0) + 0.6T_e(\tau)t/\tau_{iE}$, since $T_e(t \gtrsim \tau) \approx T_e(\tau) \gg T_i(\tau)$ and $C_e/(C_e + C_i) \approx 0.6$ for $K_B T_e \sim E_F$.

The dielectric permittivity ε given by Eq. (5) contains the contribution from both the interband and intraband absorption mechanisms

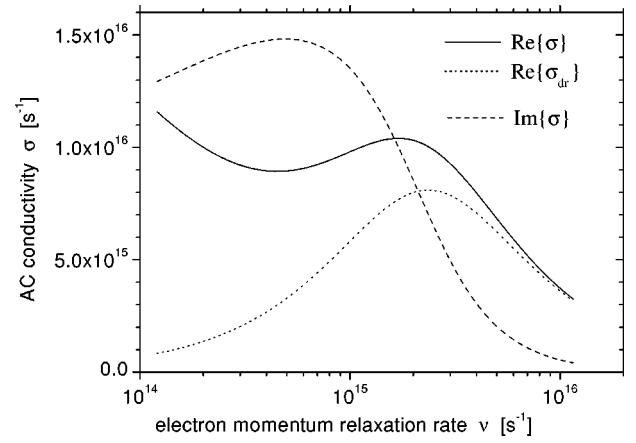
$$\sigma = \sigma_{\text{Dr}} + \sigma_{b-b}, \quad (19)$$

where the subscript ‘‘Dr’’ stands for the intraband (‘‘Drude,’’ i.e., inverse bremsstrahlung) absorption described by

$$\sigma_{\text{Dr}} = \frac{n_e e^2}{m_{\text{opt}}} \frac{\nu + i\omega}{\nu^2 + \omega^2}, \quad (20)$$

and ‘‘b-b’’ stands for interband (‘‘band-band’’) absorption. The interband transitions considered here occur between the Bloch electron bands. In metals with (partially) occupied atomic d subshells, a different class of interband transitions is also possible, namely, the transitions between the occupied d states and the Fermi surface. That type of interband transitions was considered in [12].

Near the faces of the first Brillouin zone in aluminum, the lower (first) and the upper (second) one-electron bands are nearly parallel, i.e., the interband transition energy is nearly independent of the electron quasimomentum. This gives rise to a ‘‘parallel-band’’ (PB) interband absorption with pronounced peaks at wavelengths about 800 and 2500 nm (the transition energy near two distinct zone face types is different). Towards the first Brillouin zone center, the interband transition energy grows significantly. This produces a ‘‘normal’’ interband absorption continuum at shorter wavelengths. σ_{b-b} includes the contribution from both the PB and the normal interband absorption. The lattice properties do not change significantly during the fs laser pulse considered here, therefore the only mechanism by which σ_{b-b} is affected by an increase in T_e and T_i is the increase in ν . The latter

FIG. 3. Dependence of σ on ν .

results in the broadening of the PB absorption peak [24]. The expressions for the real and imaginary parts of σ_{b-b} are derived in Ref. [25] (expressions (19) and (22) *ibid.*, the latter being taken with the opposite sign in the present notation). As we said, σ_{b-b} depends on T_e and T_i only through ν ; the latter is denoted $1/\tau_{\text{bulk}}$ in [25]. Figure 3 shows real and imaginary parts of σ , as functions of ν , for $\omega = 2.355 \times 10^{15} \text{ s}^{-1}$ (wavelength $\lambda = 800 \text{ nm}$). In aluminum at room temperature for visible and near-infrared radiation, $\text{Re}\{\sigma_{b-b}\}$ is significantly larger than $\text{Re}\{\sigma_{\text{Dr}}\}$, and the dominant light absorption mechanism is interband [15]. The interband absorption peak lies at $\lambda \approx 800 \text{ nm}$. For shorter λ 's (larger ω 's) both $\text{Re}\{\sigma_{b-b}\}$ and $\text{Re}\{\sigma_{\text{Dr}}\}$ decrease rapidly with ω , the interband mechanism remaining dominant throughout the visible region. As the temperature increases, $1/\tau_{\text{bulk}} = \nu$ increases and the PB interband absorption line profile becomes broader. This corresponds to a decrease in the interband absorption in the vicinity of the 800 nm peak. By contrast, Drude absorption increases with temperature. For fs-laser pulses of relatively low energy, T_e and T_i stay sufficiently low for the decrease in the interband absorption not to be compensated by an increase in the Drude absorption. Thus, the average absorption coefficient A , Eq. (7), for 800 nm fs-laser pulse *decreases* with an increase in peak intensity, and is *lower* than the room-temperature A value. For 50 fs 800 nm pulses, A reaches minimum at $I_0 \approx (1-2) \times 10^{13} \text{ W/cm}^2$. For higher intensities, Drude absorption dominates, and $A(I_0)$ grows rapidly, exceeding its room-temperature value for $I_0 > 5 \times 10^{13} \text{ W/cm}^2$. Figure 4 shows the temporal evolution of T_e and T_i in the vicinity of the irradiated target surface for various pulse peak intensities. For pulses during which T_e on the target surface reaches 2–3 eV, the Drude absorption becomes dominant and A starts to grow rapidly with pulse intensity (for constant pulse duration). This trend lasts for intensities of up to 10^{15} W/cm^2 . It is also important to note that ε varies strongly on the spatial scale of order of the skin depth. These gradients of ε also affect the absorption coefficient value, and therefore it is important to solve Eqs. (3) and (4) to obtain accurate values of A .

At the shoulders of the PB absorption line, few tens of nanometers in either direction from the 800 nm peak, only a

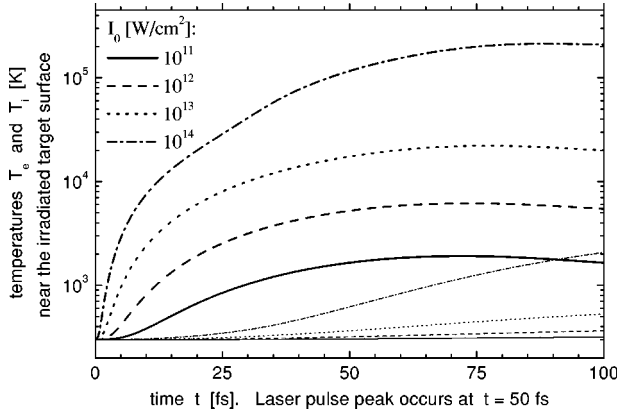


FIG. 4. Dependence of T_e (thick lines) and T_i (thin lines) on t during a 800 nm 50 fs laser pulse, for various values of I_0 . Note that during most of the pulse $T_e \gg T_i$ for every I_0 shown.

substantial broadening of the absorption line can produce a decrease in the PB absorption strong enough to compete with the increase in the intraband absorption as I_0 is increased. Thus, at certain wavelengths (e.g., near 750 nm) we predict an initial increase in A at $I_0 \lesssim 10^{12}$ W/cm², then, at $I_0 \sim 5 \times 10^{12}$ W/cm²—the decrease described above, and for I_0 between 10^{13} and 10^{15} W/cm²—again an increase. The ε -gradient effect on A becomes especially important in this case.

In the present paper, we describe the target material as an ordered system, i.e., retaining a crystal structure throughout the laser-pulse duration. Now that we have found the expressions for the coefficients of Eqs. (1)–(5), we can complete the verification of the consistency of this description. We have already shown that the crystal structure of the skin layer of the aluminum sample irradiated by a 50 fs laser pulse with $I_0 \lesssim 10^{14}$ W/cm² is affected neither by the electron-impact ionization nor by the free-surface expansion during the irradiation times. However, as mentioned above, there exists a third mechanism of destruction of the lattice order, namely, the ultrafast melting. In metals, the ultrafast melting does not occur before the lattice (phonon) temperature $T_i(t)$ reaches the melting temperature T_{melt} of the respective solid phase at the room pressure. Having this in mind, we have evaluated, using Eqs. (1)–(5), $T_i(t)$ at various depths within the target, as a function of I_0 . This allowed us to find the time $t_{melt}(x)$, given by equation $T_i(t_{melt}) = T_{melt}$, which presents a lower limit on the time at which the ultrafast melting occurs at the given depth x inside the target. Of course, t_{melt} is a functional of $I(t)$ for $-\infty < t \leq t_{melt}$. In Fig. 5, we present the results for t_{melt} in a $\lambda = 800$ nm laser pulse with the temporal profile given by Eq. (6), where $\tau = 50$ fs. The pulse starts at $t = 0$ and ends at $t = 2\tau = 100$ fs, therefore, the processes taking place in the target at $t > 100$ fs do not affect the absorption coefficient A for the laser pulse. One can readily see that for $I_0 \leq 4 \times 10^{13}$ W/cm², there can be no ultrafast melting even in the hottest surface layer throughout the laser pulse duration. The results for t_{melt} in a 400 nm 50 fs laser pulse are quite similar to those shown in Fig. 5. On both wavelengths, the effect of the ultrafast melting on the absorption of the laser pulse may become significant only for I_0

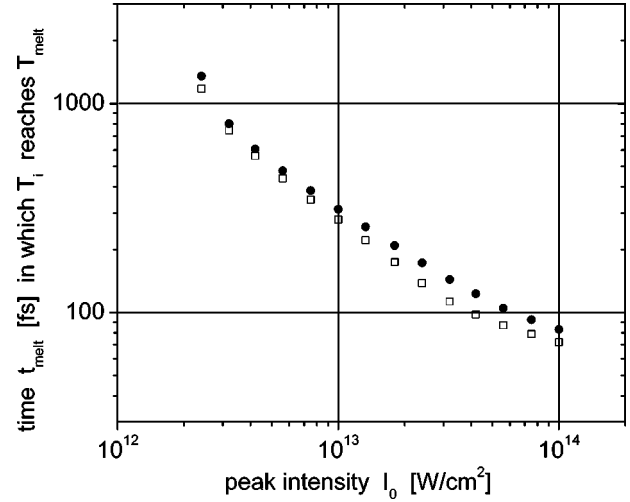


FIG. 5. Lower limit on the ultrafast melting onset time. Open squares correspond to the surface layers ($x \leq 1$ nm), filled circles correspond to the layer at the depth $x = 10$ nm below the irradiated target surface.

$> 10^{14}$ W/cm², i.e., outside the intensities range $0 < I_0 < 10^{14}$ W/cm², which we consider in the theoretical part of our paper. This prediction is in good agreement with the evidence found in literature. Even in semiconductors, where the ultrafast melting can be nonthermal, the melting occurs more than 100 fs *after* the electrons are heated to a temperature of several electron volts [26–29]. The ultrafast melting in metal was observed so far only by Wang and Downer [11], using a pump-probe technique, with a 1 ps resolution.

We note that in order to evaluate $t_{melt}(I_0)$ accurately, we have increased the precision of the expression for U compared to Eq. (12). This was achieved by preserving the logarithmic factor, equivalent to the one that is expanded to obtain the expression (6) of Ref. [19], and performing the integrations numerically. As the result, the predicted τ_{iE} values did not noticeably change for $T_e \lesssim 3$ eV (the expansion

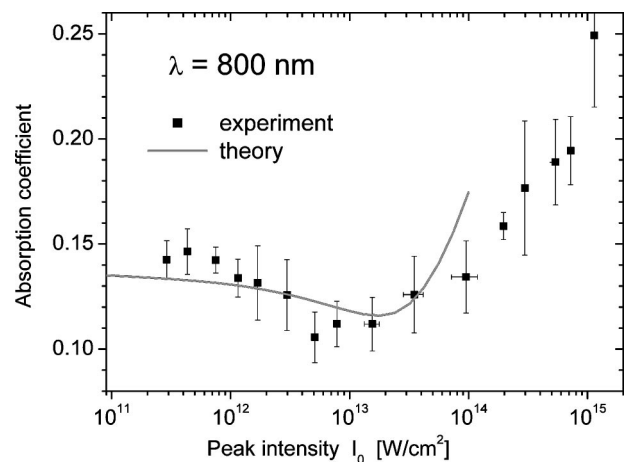


FIG. 6. Comparison of the experimental results with the theoretical predictions for 800 nm wavelength. The theory is valid only as far as the ionic structure within ~ 10 nm target surface layer remains intact, i.e., for I_0 up to 10^{14} W/cm².

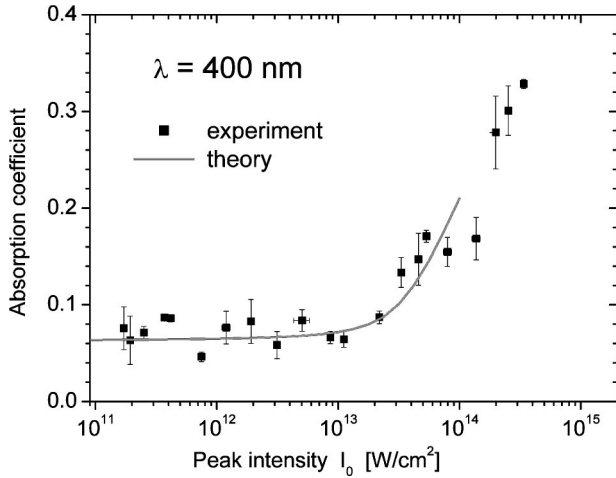


FIG. 7. Comparison of the experimental results with the theoretical predictions for 400 nm wavelength.

is exact for low T_e), but increased somewhat for larger T_e (by 70% for $T_e = 20$ eV) in comparison to those shown in Fig. 2 above. This precision improvement has a negligible effect on A (at $T_e \geq 3$ eV, the e-e collisions and the intraband absorption are dominant anyway), therefore, we recommend to use the analytic expression (12) for calculation of the optical properties.

III. EXPERIMENT

Experimental measurements of the absorption coefficient A in aluminum as a function of peak laser intensity I_0 were conducted using the Soreq high-intensity (10 TW) short-pulse laser facility. The Ti:Sapphire oscillator produces a 74 MHz train of about 20 fs pulses with spectral width of 45 nm around $\lambda = 800$ nm and with an average power of about 0.4 Watt (5 nJ per pulse). A Pockels-cell based pulse picking device selects only the pulses to be amplified, at a repetition rate of 10 Hz. These pulses are stretched by an all-reflective aberration-free stretcher to a pulse width of about 0.2 ns. After amplification in a regenerative amplifier, another Pockels cell is used to clean the pulse from pre- and post pulses. The second and third amplification stages are four-pass amplifiers, boosting the pulse energy to ~ 35 and > 800 mJ, respectively. The pump sources are Nd:YAG lasers operating at 10 Hz in second-harmonic generation with total pumping energy of 2.5 J per pulse. Gain narrowing reduces the spectral bandwidth to about 25 nm. A high efficiency ($\sim 57\%$) parallel grating compressor is used to recompress the pulses to 45 fs, producing 10 TW pulses at 10 Hz (450 mJ per pulse). Nanosecond and picosecond prepulses were measured using high-dynamic range photodetector and third-order autocorrelator, respectively. The use of the pulse picker and pulse cleaner modules allows us to obtain the prepulse-to-pulse contrast ratio better than $1:10^5$. To produce 400 nm radiation, a thin (0.3 mm) BBO crystal was used, with conversion efficiency of a few tens of percent (intensity dependent).

The laser is focused on the target by a $f/10$ lens, at 0° . The focal diameter is $70 \mu\text{m}$ for $\lambda = 800$ nm and $60 \mu\text{m}$

for $\lambda = 400$ nm. A charge-coupled camera is used to monitor a fraction of the beam in order to compensate for pulse energy variations. Intensity is varied by a set of calibrated neutral density filters. The targets are aluminum films ~ 500 nm thick, produced by a conventional low-vacuum evaporation method on optically smooth glass substrates. The target is moved between shots, so that each laser pulse hits a clean target area. A beam splitter is mounted before the lens and sends part of the specularly reflected light to a calibrated pyroelectric energy meter, located outside the vacuum chamber. The time-integrated reading of the energy meter is corrected to account for the beam splitter, lens, and vacuum-window reflections. An Ulbricht sphere was used to measure diffused reflection, but this reflection was always much less than 1% of the incident light, and was not taken into consideration.

Figure 6 presents a comparison between the experimental and the theoretical results we have obtained at $\lambda = 800$ nm. The values of A presented on Fig. 6 are averaged over the Gaussian intensity distribution in the laser focal spot on the target surface. The intensity I_0 specified corresponds to the spot center. At room temperature, for $\lambda = 800$ nm the targets have $A = 0.139$ (measured by the same setup operating in cw mode). Figure 6 shows that the agreement between the theory and the experiment is quite good, with both the theoretical and the experimental curves showing the decrease in absorption with minimum at $I_0 \sim 10^{13}$ W/cm². In the present paper this phenomenon is predicted and observed for the first time.

Figure 7 presents a comparison between the experimental and the theoretical results we have obtained at $\lambda = 400$ nm. This wavelength is located far from the PB interband absorption peaks, therefore in this case, the broadening of the aforementioned peaks does not produce a decrease in the interband absorption, and A is predicted to grow monotonously with I_0 . The experimental results agree very well with the theory.

The absence of a decrease in A in the $\lambda = 400$ nm experiment confirms our theoretical prediction that the ultrafast melting plays no role for $I_0 < 10^{14}$ W/cm². Indeed, if the ultrafast melting was contributing to the decrease in A observed in the $\lambda = 800$ nm experiment, one would expect to find A decreasing for $\lambda = 400$ nm, too, since the dependence of $T_i(x, t)$ on I_0 is quite similar for these two laser wavelengths. The comparison of the experimental results for $\lambda = 400$ and for 800 nm confirms therefore that the decrease in A observed for $\lambda = 800$ nm at $I_0 \leq 5 \times 10^{13}$ W/cm² is caused by the broadening of the PB interband absorption peak.

The difference between the predicted and the measured values of A at $\lambda = 800$ nm, $I_0 \approx 10^{14}$ W/cm², is due to the prepulse effect. Indeed, at $\lambda = 400$ nm, the pulse-to-prepulse contrast ratio is improved by the frequency doubling, and the experimental results agree well with the theory also for highest peak intensities.

We stress that the theory we have presented has no free parameters to fit the experimental curves. The parameters characterizing the electron and phonon spectra and interaction in metallic aluminum are all found from the published data on room-temperature properties and dc conductivity of aluminum.

IV. SUMMARY

We have presented a comprehensive theoretical description for the absorption of the normally incident ultrashort laser pulses in metal, and provided the experimental verification for our results in aluminum. The mechanisms of momentum and energy relaxation are considered, and the expressions for the respective relaxation times are obtained. The thresholds and the time scales for the processes leading to the destruction of the lattice order are given.

We have demonstrated, both theoretically and experimentally, that the interplay between the inter- and the intraband absorption mechanisms in a metallic target irradiated by fs-laser pulses of near-infrared or visible radiation can lead to a significant *reduction* in the absorption coefficient compared to its room-temperature value. In aluminum, this phenomenon takes place for radiation peak intensities up to 5×10^{13} W/cm², for the wavelengths between 750 and 870 nm, and is strongest near 800 nm.

It is important to stress the following three points pertaining to the formulation of the mathematical model, Eqs. (1)–(5). First, the dielectric permittivity at the laser radiation frequency is often dominated by interband transitions term rather than by the intraband transitions (inverse bremsstrahlung) term. This is important for short (tens of fs) laser pulses of moderate intensity ($I_0 \leq 10^{13}$ W/cm²), when the

crystal structure of target metal at the depths of order of a skin depth remains intact during the laser pulse. Second, it is crucial to account for both e-e and e-ph collisions in the determination of electron momentum relaxation rate. In many theoretical treatments found in literature, only e-ph collisions are taken into account, while in reality, the role of e-e collisions in the radiation absorption is essential. Moreover, for the above conditions the role of e-ph collisions is only secondary. Indeed, as we have shown above, in Al for $T_e \leq 1$ eV, the laser radiation absorption occurs mostly in interband transitions, while for $T_e \geq 3$ eV, the absorption is mostly due to collisions between electrons. Finally, the third point we would like to stress is the importance of solving directly the Helmholtz Eq. (4) rather than using simple approximations based on Fresnel formula. Indeed, due to the interplay between various contributions to ϵ , the complex refraction index changes strongly and nonmonotonously on the distance of order of the skin depth from the irradiated target surface inwards. These spatial variations have a strong effect on the absorption coefficient.

ACKNOWLEDGMENT

The authors acknowledge valuable discussions with Y.B. Levinson.

-
- [1] S. I. Anisimov *et al.*, Zh. Tekh. Fiz. **36**, 1273 (1966) [Sov. Phys. Tech. Phys. **11**, 945 (1967)].
 - [2] S. I. Anisimov, B. L. Kapeliovich, and T. L. Perel'man, Zh. Eksp. Teor. Fiz. **66**, 776 (1974) [Sov. Phys. JETP **39**, 375 (1974)].
 - [3] J. G. Fujimoto, J. M. Liu, E. P. Ippen, and N. Bloembergen, Phys. Rev. Lett. **53**, 1837 (1984).
 - [4] H. M. Milchberg, R. R. Freeman, S. C. Davey, and R. M. More, Phys. Rev. Lett. **61**, 2364 (1988).
 - [5] H. M. Milchberg and R. R. Freeman, J. Opt. Soc. Am. B **6**, 1351 (1989).
 - [6] S. I. Anisimov and B. Rethfeld, Proc. SPIE **3093**, 192 (1997).
 - [7] S. Nolte *et al.*, J. Opt. Soc. Am. B **14**, 2716 (1997).
 - [8] A. P. Kanavin *et al.*, Phys. Rev. B **57**, 14 698 (1998).
 - [9] D. F. Price *et al.*, Phys. Rev. Lett. **75**, 252 (1995).
 - [10] L. Spitzer, *Physics of Fully Ionized Gases* (Interscience, New York, 1956).
 - [11] X. Y. Wang and M. C. Downer, Opt. Lett. **17**, 1450 (1992).
 - [12] C.-K. Sun *et al.*, Phys. Rev. B **50**, 15 337 (1994).
 - [13] K. Eidmann, J. Meyer-ter-Vehn, T. Schlegel, and S. Hüller, Phys. Rev. E **62**, 1202 (2000).
 - [14] N. W. Ashcroft and N. D. Mermin, *Solid State Physics* (Saunders, Philadelphia, 1976).
 - [15] D. Y. Smith, E. Shiles, and M. Inokuti, *The Optical Properties of Metallic Aluminum*, in *Handbook of Optical Constants of Solids*, edited by E. D. Palik (Academic, New York, 1985).
 - [16] V. E. Zinov'ev, *Handbook of Thermophysical Properties of Metals at High Temperatures* (Nova Science Publisher, New York, 1996).
 - [17] R. D. Cowan, *The Theory of Atomic Structure and Spectra* (University of California Press, Berkeley, 1981).
 - [18] V. A. Bernshtam, Yu. V. Ralchenko, and Y. Maron, J. Phys. B **33**, 5025 (2000).
 - [19] M. I. Kaganov, I. M. Lifshitz, and L. V. Tanatarov, Zh. Eksp. Teor. Fiz. **31**, 232 (1956) [Sov. Phys. JETP **4**, 173 (1957)].
 - [20] V. F. Gantmakher and Y. B. Levinson, *Carrier Scattering in Metals and Semiconductors* (North-Holland, Amsterdam, 1987).
 - [21] P. H. Dederichs, H. R. Schober, and D. J. Sellmyer, in *Landolt-Börnstein Numerical Data and Functional Relationships in Science and Technology—New Series*, Group III, Vol. 13a, edited by K.-H. Hellwege and J. L. Olsen (Springer-Verlag, Berlin, 1981), p. 11.
 - [22] A. P. Cracknell, in *Landolt-Börnstein Numerical Data and Functional Relationships in Science and Technology—New Series*, Group III, Vol. 13c, edited by K.-H. Hellwege and J. L. Olsen (Springer-Verlag, Berlin, 1984), p. 36.
 - [23] A. A. Abrikosov, *Introduction to the Theory of Normal Metals* (Academic Press, New York, 1972).
 - [24] For $T_e \geq E_F$ additional changes in σ_{b-b} follow from the increased population of the higher bands. However, at such temperatures the interband absorption is negligible compared to Drude absorption.
 - [25] N. W. Ashcroft and K. Sturm, Phys. Rev. B **3**, 1898 (1971).
 - [26] P. L. Silvestrelli, A. Alavi, M. Parrinello, and D. Frenkel, Phys. Rev. Lett. **77**, 3149 (1996).
 - [27] D. H. Reitze, H. Ahn, and M. C. Downer, Phys. Rev. B **45**, 2677 (1992).
 - [28] P. Stampfli and K. H. Bennemann, Phys. Rev. B **49**, 7299 (1994).
 - [29] K. Sokolowski-Tinten *et al.*, Phys. Rev. B **58**, R11 805 (1998).